Pore size effect on high-efficiency proton conduction in three stable 3D Al-based MOFs modified with imidazole

Lu Zhang, [‡a] Xiaoxue Ma, [‡a] Xin Li, [a] Ronghua Liu, [a] Xin Zhao, [a] Hongguo Hao, [a]*

Hui Yan, [a] Hongjie Zhu, [a] Huawei Zhou, [a] Dichang Zhong [b]*

[a]Shandong Provincial Key Laboratory of Chemical Energy Storage and Novel Cell Technology, School of Chemistry and Chemical Engineering, School of Pharmacy, Liaocheng University, Liaocheng 252059, China.

[b]Institute for New Energy Materials and Low Carbon Technologies School of Materials Science and Engineering Tianjin University of Technology, Tianjin 300384, China.

‡ Lu Zhang and Xiaoxue Ma contributed equally to this work.

* Corresponding Authors E-mail: hhg207@126.com; yanhui@lcu.edu.cn

Supplementary Information

Contents

1. Materials and Instrumentations.

All reagents and solvents were obtained commercially and used without any purification. The powder X-ray diffraction patterns (PXRD) were recorded on a Rigaku D/Max-2500 diffractometer and the intensity data were recorded by continuous scan in a 2θ mode from 3 to 50°, with a step size of 0.1 and a scan speed of 20 min^{-1}. The simulated PXRD patterns were produced using the Mercury V1.4 program and single-crystal diffraction data. A PerkinElmer Diamond SII thermal analyzer was utilized for Thermogravimetric analysis (TGA) tests from 298 to 1073 K, at a heating rate of 10 K min^{-1} under a nitrogen atmosphere. Infrared spectra were recorded on a Nicolet 6700 FT-IR spectrophotometer with KBr pellets in the range 4000-400 cm^{-1} region. X-ray photoelectron spectroscopy (XPS) characterization was carried out by using a Thermo-Fisher Scientific ESCALAB spectrometer with Al $K\alpha$ X-rays (1486.6 eV) as the light source and the C1s peak at 284.6 eV as internal standard. Element distribution was characterized by Hitachi SEM S-4800. Energy-dispersive X-ray spectroscopy (EDS) and element mapping analyses were recorded on a Thermo-Fisher Scientific FIB-SEM GX4. Nitrogen adsorption-desorption isotherms were measured at 77 K on micromeritics 3Flex were measured at 298 K.

2. Material Synthesis and Structure.

Three Al-MOFs, **DUT-5 (1)**, **DUT-4 (2)**, and **NOTT-300(Al) (3)**, were prepared in light of the early literature methods. CCDC 691979 (for **1**) 691978 (for **2**), and 1856081 (for **3**) contain the supplementary crystallographic data for this paper. These datas can be obtained free of charge from The Cambridge Crystallographic Data Centre.

2.1 Synthesis of 1.

4,4-biphenyldicarboxylic acid also known as H$_2$BPDC linker (97%, 0.26 g, 1.20 mmol) was dissolved in 30 mL DMF (Fischer, analytical reagent grade). Al(NO$_3$)$_3$.9H$_2$O (98%, 0.52 g, 1.40 mmol) was added and the mixture was filled in a 250 mL Teflon liner, placed in an autoclave, heated to 120 °C for 24 h and cooled to room temperature. After the product was separated by centrifugation, the sediment was washed with DMF for three times. The product was dried in an oven. 0.49 g (95.6%)

for **1**. [Al(OH)(C$_{14}$O$_4$H$_8$)(DMF)$_{1.8}$](H$_2$O)$_{3.6}$: calc (%): C, 49.68; H, 3.03; N, 5.54, found (%): C, 49.60; H, 3.09; N, 5.51. FT-IR (4000-400 cm^{-1}): 3404 (m), 3140 (w), 1657 (m), 1598 (m), 1546 (m), 1400 (s), 1178 (w), 1104 (w), 1053 (w), 1009 (w), 854 (w), 774 (m), 501 (w).

2.2 Synthesis of 2.

First, a solution of 2,6-naphthalene dicarboxylic acid, also known as H$_2$NDC linker (95%, 0.26 g, 0.83 mmol) in N, N-dimethylformamide (DMF, 30 mL) was mixed with nonahydrate aluminum nitrate Al(NO$_3$)$_3$·9H$_2$O (98%, 0.52 g, 1.40 mmol) in a Teflon Liner. Then, the liner was placed into an autoclave at 120 °C for 24 h. After that, the autoclave was opened at room temperature, and the product was washed with 20 mL of DMF and centrifuged for 2.5 min at 10000 rpm three times. Finally, the product was dried for 4 h at 120 °C in an oven. Yield: 0.43 g (90.5%) for **2**. [Al(OH)(C$_{12}$O$_4$H$_6$)(DMF)$_{1.3}$](H$_2$O)$_{1.4}$: calc (%): C, 47.85; H, 5.37; N, 4.73, found (%): C, 47.80; H, 5.41; N, 4.69. FT-IR (4000-400 cm^{-1}): 3534 (m), 3110 (w), 1631 (m), 1549 (m), 1541 (m), 1407 (s), 1159 (w), 1112 (w), 1067 (w), 1015 (w), 874 (w), 770 (m), 515 (w).

2.3 Synthesis of 3.

In a typical procedure, Al(NO$_3$)$_3$·9H$_2$O (0.34 g, 0.906 mmol), biphenyl-3,3′,5,5′-tetracarboxylic acid (0.06 g, 0.182 mmol) and piperazine (0.10 g, 1.26 mmol) were mixed and dispersed in ultrapure water (10 mL), then HNO$_3$ (2.8 M, 2 mL) was added to the resulting mixture. After stirring for 30 min, the milky slurry was transferred into a 25 mL lining of polytetrafluoroethylene reactor, which was sealed in the autoclave and heated to 210 °C for 72 h. After cooling overnight to room temperature, the resultant white microcrystalline product was separated by filtration, washed several times with water and dried overnight in an oven at 60 °C. The as-prepared solid sample was activated in two steps: the initial product was first immersed in nitric acid solution for 24 h to remove unreacted species; in the second step, ethanol was used to exchange guest molecules in pores of **3**, by sealing in an autoclave and heating at 100 °C for 20 h. The resultant white solid product was separated by filtration, washed several times

with ethanol and dried overnight in an oven at 60 °C. $[Al(OH)(C_{16}O_8H_6)_{0.5}](H_2O)_7$: calc (%): C, 35.37; H, 3.39; N, 0.00, found (%): C, 35.34; H, 3.44; N, 0.00.

2.4 Synthesis of Im@1-3.

The activated samples of **1-3** were immerged in 1.0 M methanol solution of imidazole for 72 h, respectively. The crystals are then dried under vacuum oven at 70 °C to obtain the imidazole-supported products Im@**1-3**.

3. Proton Conduction Measurement.

The alternating-current (AC) impedance plots were recorded on a CHI660E impedance analyzer (AC voltage = 100 mV; frequency = $1\text{-}10^6$ Hz) with a quad four-probe electrochemical cell. The microcrystalline powder of relevant MOFs (80-100 mg) was pressed under the pressure of 2.5~3.0 MPa, and the cuboid sample was obtained. See Figure S13, the size of the sample was 1.01 cm × 0.42 cm × 0.26 cm measured by vernier caliper. Different RHs (45-100%) and temperatures (20-80 °C) were applied.

The impedance spectra were recorded under different relative humidity and temperature, wherein the relative humidity (RH) was controlled using the standard saturated aqueous solutions of certain salts. The relative humidity inside the chamber was controlled by standard saturated aqueous solutions of pure water, $NaSO_4$, KCl, NaCl, NaBr, and K_2CO_3 (corresponding RH are about 100, 93, 86, 75, 60, and 45%, respectively). Consequently, both sides of the plate were attached to silver wires with silver paste and then put in a sealed double walled glass chamber and connected to the electrochemical workstation. The proton conductivities of the plate were then tested by a quasi-four-probe method in the chamber connected with a temperature-controlled circulation water bath. The cuboid sample was fully hydrated in the corresponding humidity for 16 h before the ac testing. All impedance data were obtained through the Power Suite program. The impedance measurements were carried out by using a CHI660E electrochemical workstation with tuned frequencies from 1.0 Hz to 4.0 MHz and alternating potentials of 100 mV. We used Zview software to fit the impedance values to obtain the equivalent circuits of the two composites to calculate the resistance.

Conductivity was deduced from the Bode diagram as well as from the Nyquist plot for comparison using the equation:

$$\sigma = \frac{L}{RS}$$ …………………………………………………….. **(eq S1)**

where L (cm) is the length of the block, R (Ω) is the impedance, and S (cm^2) is the face area of the plate (S = thickness × width). All measurements were repeated three times to get reproducible results. The activation energy (E_a) was calculated by the equation (2) in previous literature.

$$\sigma T = \sigma_0 \exp\left(\frac{-E_a}{k_B T}\right)$$ …………………………………………….... **(eq S2)**

where σ is the proton conductivity, σ_0 is the preexponential factor, k_B is the Boltzmann constant, and T is the temperature (K). E_a is the activation energy (eV).

4. The Grand Canonical Monte Carlo Simulations.

The Grand Canonical Monte Carlo (GCMC) simulations were performed for H_2O and imidazole adsorption on **1-3**. The MOF skeletons were both treated as rigid bodies. The beneficial adsorption sites were simulated by the fixed loading task and Metropolis method at 298 K and 100 kPa. The loading steps, equilibration steps and the production steps were all set to 2.0×10^7. The saturation/maximum uptakes were modeled at 298 K using the fixed pressure task and Metropolis method with 2.0×10^7 equilibration steps, followed by 2.0×10^7 production steps for calculating the ensemble averages. The dispersive and steric repulsive interactions of each atom in **1-3** frameworks and water molecules were both modeled by the dreiding force field (Dreiding) or universal force field (UFF). The atomic partial charges of the framework were used for Q_{eq} method, the guest gas molecules were optimized using the DMol3 method and adopted the B3LYP fitted charge. The interaction between the guest water, imidazole molecule and the MOF structure is described by the Lennard-Jones (LJ) contribution and the cut-off radius used for the Lennard-Jones interactions is 12.8 Å. All the simulations were carried out by using sorption module in the Material Studio software.
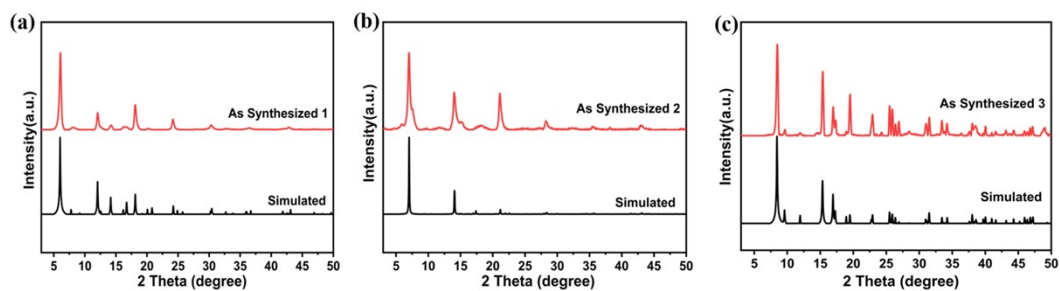
5. AC Impedance Analysis.

Figure S1. Powder X-ray diffraction patterns of MOFs: (a) **1**, (b) **2**, (c) **3**.
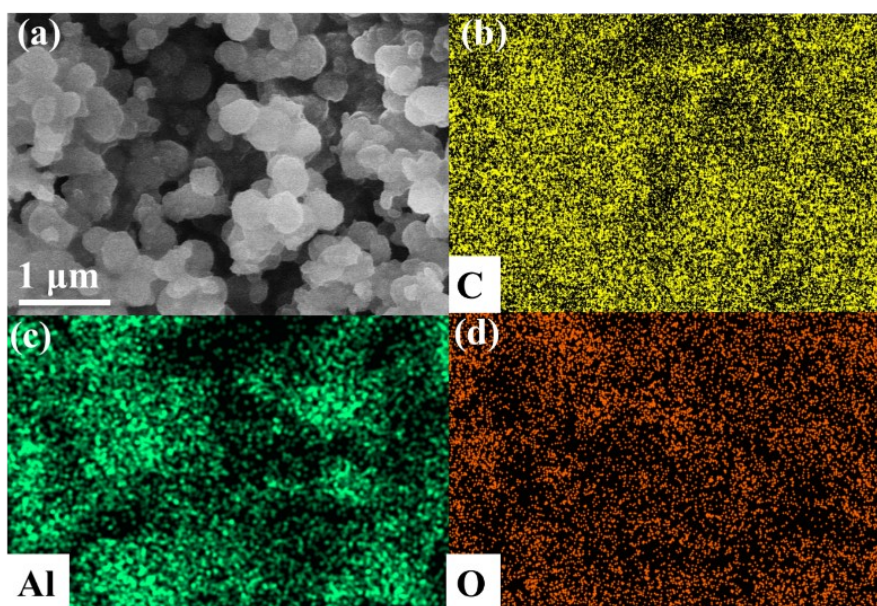
Figure S2. SEM image and energy-dispersive elemental mapping images of MOF **1**.
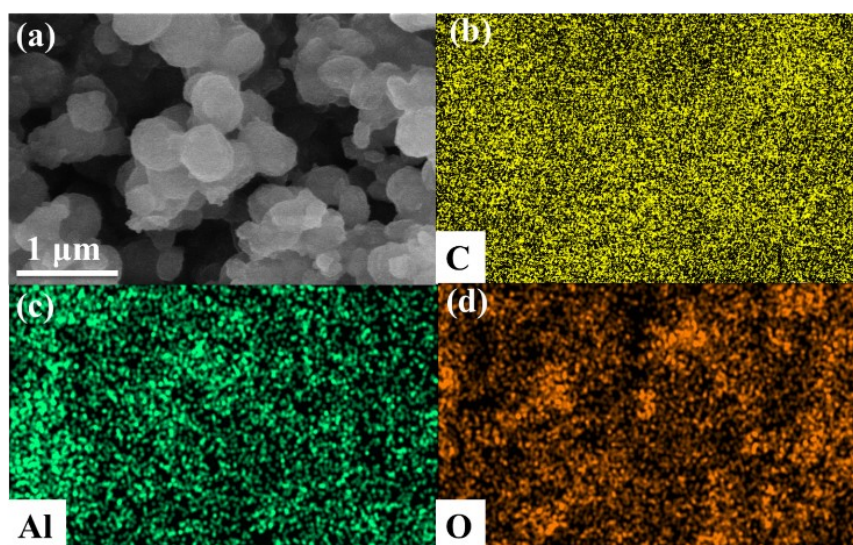
Figure S3. SEM image and energy-dispersive elemental mapping images of MOF **2**.
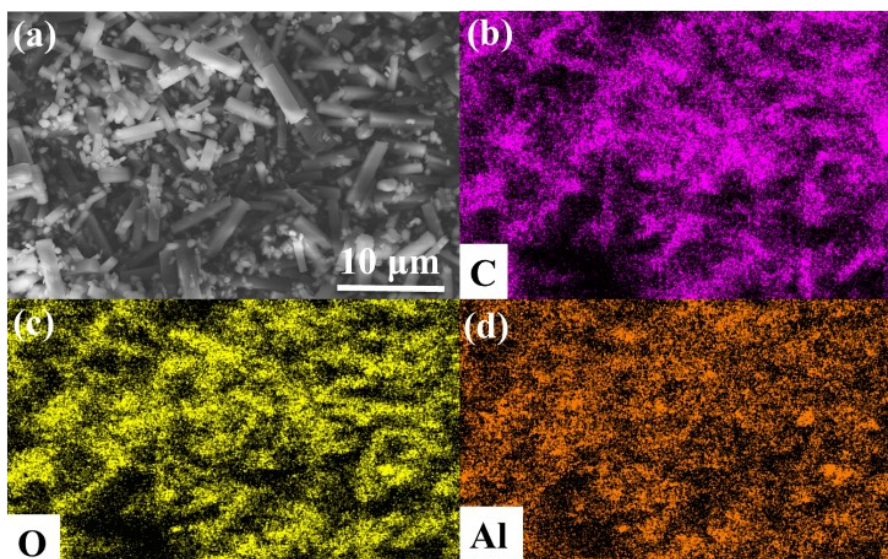
Figure S4. SEM image and energy-dispersive elemental mapping images of MOF **3**.
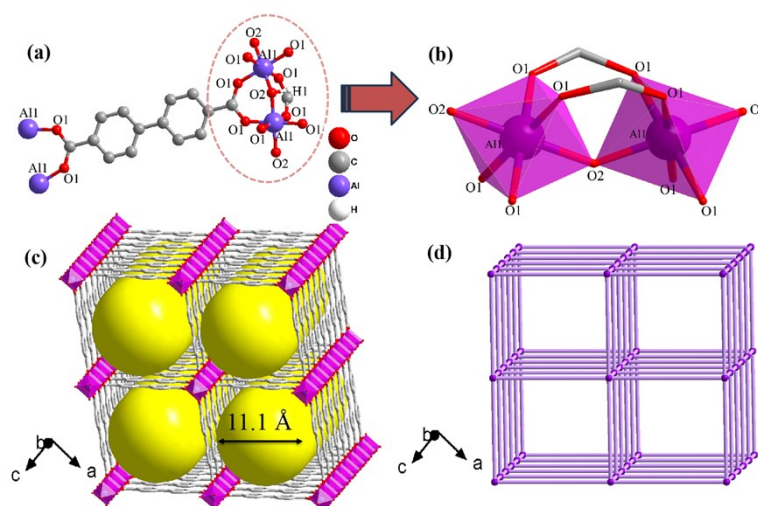
Figure S5. (a) Simplified coordination environments of **1** $[Al(OH)(C_{14}O_4H_8)(DMF)_{1.8}](H_2O)_{3.6}$. (b) Coordination environment of a binuclear Al_2 SBU. Color code: C, gray; O, red; Al, purple; H, white. The H atoms are omitted. (c) The one-dimensional channel structure of the three-dimensional framework is observed from the *b* axis. (d) The simplified topology structure of **1**.
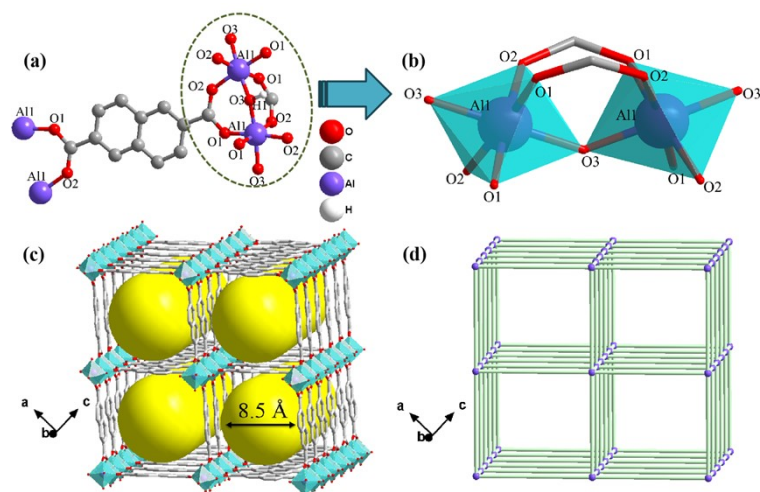
Figure S6. (a) Simplified coordination environments of **2** $[Al(OH)(C_{12}O_4H_6)(DMF)_{1.3}](H_2O)_{1.4}$. (b) Coordination environment of a binuclear Al_2 SBU. Color code: C, gray; O, red; Al, purple; H, white. The H atoms are omitted. (c) The one-dimensional channel structure of the three-dimensional framework is observed from the *b* axis. (d) The simplified topology structure of **2**.
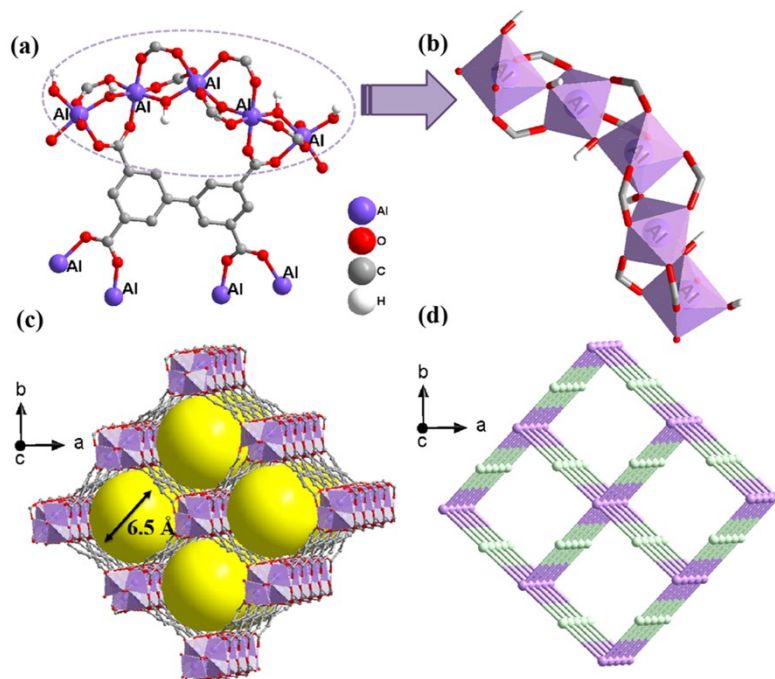
Figure S7. (a) Simplified coordination environments of **3** $[Al(OH)(C_{16}O_8H_6)_{0.5}](H_2O)_7$. (b) Coordinated environment of aluminum metal clusters. Color code: C, gray; O, red; Al, purple; H, white. The H atoms are omitted. (c) The one-dimensional channel structure of the three-dimensional framework is observed from the *c* axis. (d) The simplified topology structure of **3**.
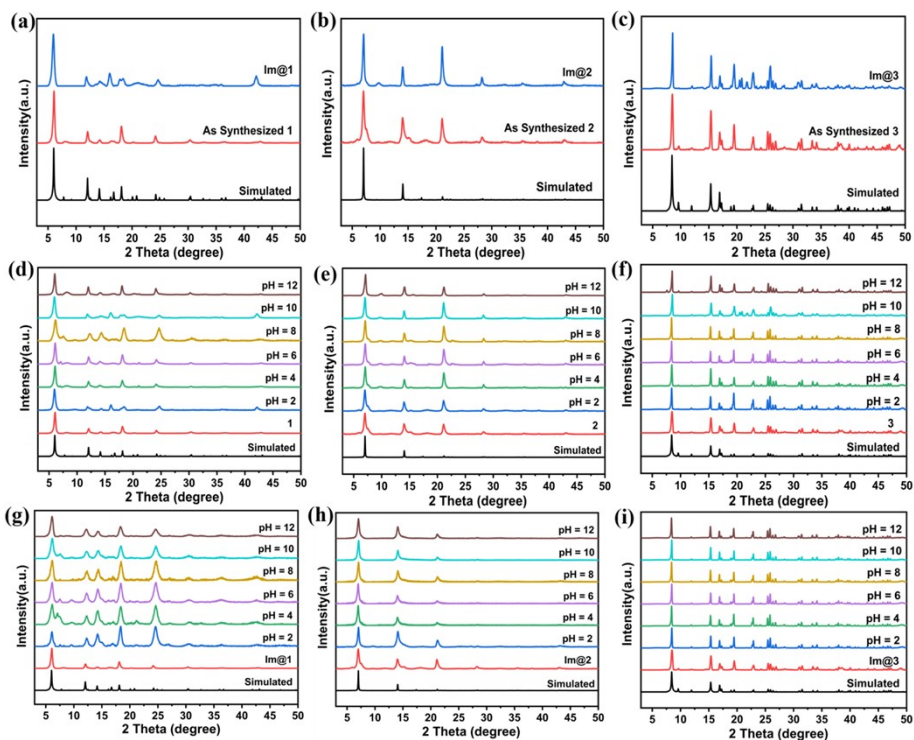
Figure S8. PXRD patterns of simulated, synthesis **1-3** and Im@**1-3** (a)-(c). PXRD patterns of **1-3** (d)-(f), and Im@**1-3** (g)-(i) at immersed in aqueous solutions of different pH values for 24 h.
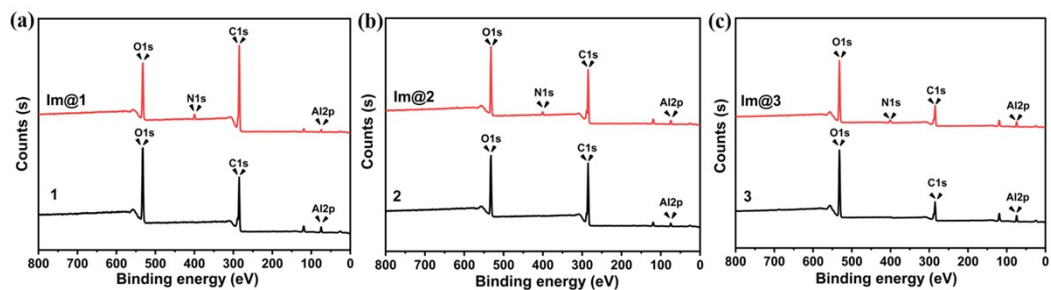
Figure S9. (a) XPS spectra of **1** and Im@**1** (a); **2** and Im@**2** (b); **3** and Im@**3** (c).
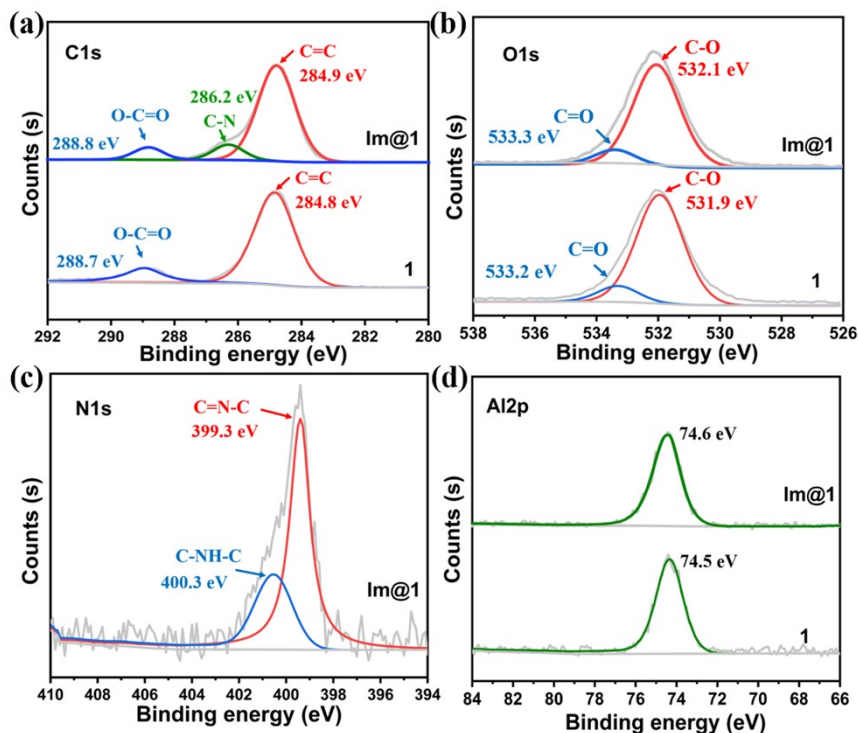
Figure S10. XPS spectra of (a) C1s, (b) O1s, (c) N1s, and (d) Al2p in **1** and Im@**1**.
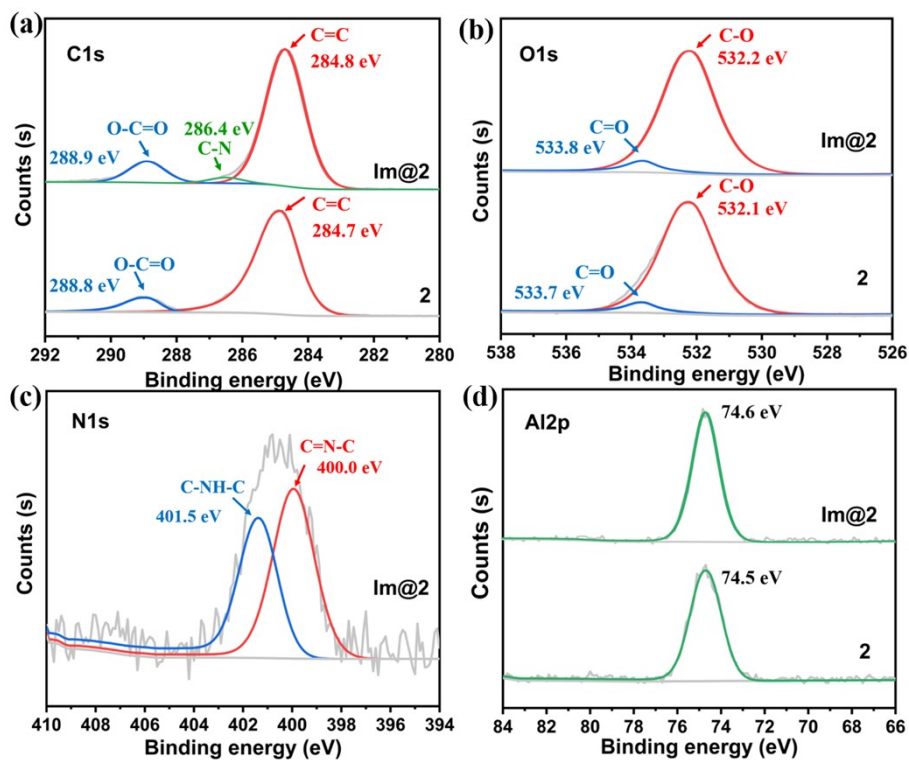
Figure S11. XPS spectra of (a) C1s, (b) O1s, (c) N1s, and (d) Al2p in **2** and Im@**2**.
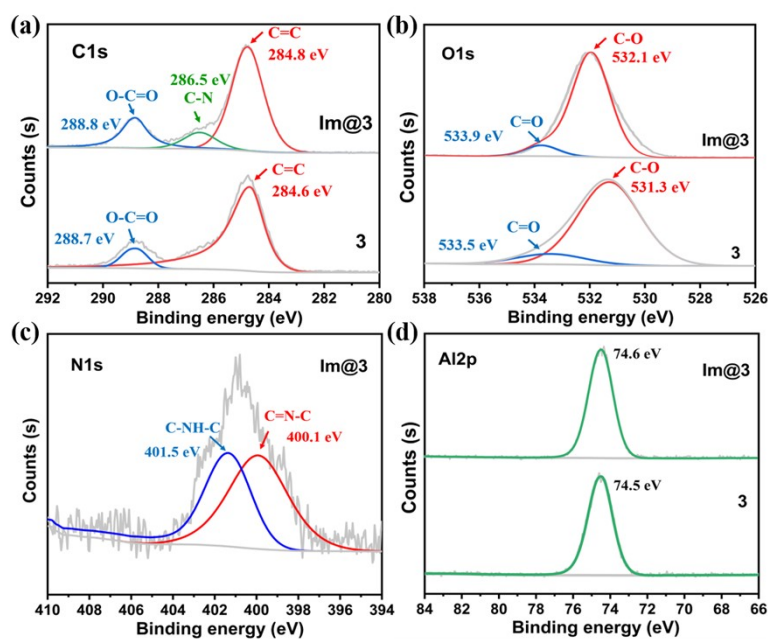
Figure S12. XPS spectra of (a) C1s, (b) O1s, (c) N1s, and (d) Al2p in **3** and Im@**3**.

Table S1. The binding energy (eV) of the characteristic peaks (C1s, O1s, N1s, and Al2p) of the XPS spectra in **1-3** and Im@**1-3**

Orbital of Elements	Functional groups	1	Im@1	2	Im@2	3	Im@3
	O−C=O	288.7	288.8	288.8	288.9	288.7	288.8
C1s	C=C	284.8	284.9	284.7	284.8	284.6	284.8
	C−N	-	286.2	-	286.4	-	286.5
	C−O	531.9	532.1	532.1	532.2	531.3	532.1
O1s	C=O	533.2	533.3	533.7	533.8	533.5	533.9
	C−NH−C	-	400.3	-	401.5	-	401.5
N1s	C=N−C	-	399.3	-	400.0	-	400.1
Al2p	-	74.5	74.6	74.5	74.6	74.5	74.6

Table S2. The Langmuir surface areas, pore volumes and pore sizes of **1-3** and Im@**1-3** are correlated

Samples	Langmuir Surface Area ($m^2\ g^{-1}$)	Pore Volume ($cm^3\ g^{-1}$)	Pore Size (Å)
1	2335	0.81	11.7
2	1996	0.68	8.9
3	1130	0.43	6.8
Im@**1**	813	0.47	9.5
Im@**2**	548	0.31	7.3
Im@**3**	131	0.26	5.6
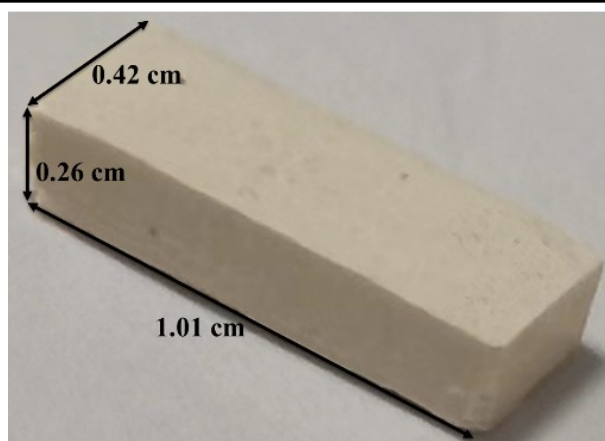
Figure S13. The photograph of the cuboid plate sample of Im@**3**. (Here, the cuboid plate takes Im@**3** as an example)

Table S3. Proton Conductivities ($S\ cm^{-1}$) of **1** at Different RHs and Temperatures

Temp (°C)	45% RH	60% RH	75% RH	85% RH	93% RH	100% RH
20	2.63×10^{-10}	7.49×10^{-7}	9.71×10^{-6}	4.12×10^{-5}	9.09×10^{-5}	2.78×10^{-3}
30	5.71×10^{-10}	1.34×10^{-6}	2.41×10^{-5}	7.23×10^{-5}	1.53×10^{-4}	3.40×10^{-3}
40	1.36×10^{-9}	2.50×10^{-6}	5.38×10^{-5}	1.23×10^{-4}	2.82×10^{-4}	4.91×10^{-3}
50	2.47×10^{-9}	5.15×10^{-6}	1.10×10^{-4}	1.97×10^{-4}	3.89×10^{-4}	6.17×10^{-3}
60	5.41×10^{-9}	7.92×10^{-6}	1.78×10^{-4}	3.12×10^{-4}	5.99×10^{-4}	8.53×10^{-3}
70	1.15×10^{-8}	1.25×10^{-5}	2.99×10^{-4}	5.51×10^{-4}	1.02×10^{-3}	1.12×10^{-2}
80	2.12×10^{-8}	2.27×10^{-5}	5.23×10^{-4}	8.46×10^{-4}	1.65×10^{-3}	1.39×10^{-2}

Table S4. Proton Conductivities ($S\ cm^{-1}$) of **2** at Different RHs and Temperatures

Temp (°C)	45% RH	60% RH	75% RH	85% RH	93% RH	100% RH
20	1.92×10^{-9}	7.02×10^{-6}	4.07×10^{-5}	2.48×10^{-4}	2.65×10^{-4}	8.38×10^{-3}

30	3.34×10^{-9}	1.09×10^{-6}	4.69×10^{-5}	3.34×10^{-4}	4.79×10^{-4}	1.10×10^{-2}
40	5.30×10^{-9}	1.69×10^{-5}	5.95×10^{-5}	4.50×10^{-4}	8.55×10^{-4}	1.28×10^{-2}
50	8.54×10^{-9}	2.88×10^{-5}	7.33×10^{-5}	5.92×10^{-4}	1.44×10^{-3}	1.74×10^{-2}
60	1.47×10^{-8}	3.81×10^{-5}	8.80×10^{-5}	7.64×10^{-4}	2.03×10^{-3}	1.98×10^{-2}
70	2.84×10^{-8}	6.26×10^{-5}	1.21×10^{-4}	1.01×10^{-3}	3.11×10^{-3}	2.48×10^{-2}
80	4.34×10^{-8}	8.90×10^{-5}	1.51×10^{-4}	1.27×10^{-3}	5.12×10^{-3}	2.98×10^{-2}

Table S5. Proton Conductivities (S cm^{-1}) of **3** at Different RHs and Temperatures

Temp (°C)	45% RH	60% RH	75% RH	85% RH	93% RH	100% RH
20	1.16×10^{-7}	9.05×10^{-5}	1.40×10^{-4}	4.53×10^{-4}	1.22×10^{-3}	1.94×10^{-2}
30	2.31×10^{-7}	1.42×10^{-4}	2.02×10^{-4}	6.04×10^{-4}	1.65×10^{-3}	2.32×10^{-2}
40	5.37×10^{-7}	2.16×10^{-4}	3.28×10^{-4}	7.09×10^{-4}	2.17×10^{-3}	2.71×10^{-2}
50	2.15×10^{-6}	3.30×10^{-4}	4.65×10^{-4}	9.06×10^{-4}	2.77×10^{-3}	3.40×10^{-2}
60	3.07×10^{-6}	4.59×10^{-4}	6.71×10^{-4}	1.25×10^{-3}	3.87×10^{-3}	4.00×10^{-2}
70	4.70×10^{-6}	6.60×10^{-4}	8.80×10^{-4}	1.67×10^{-3}	5.27×10^{-3}	4.73×10^{-2}
80	8.84×10^{-6}	9.78×10^{-4}	1.36×10^{-3}	2.38×10^{-3}	7.37×10^{-3}	5.57×10^{-2}

Table S6. Proton Conductivities (S cm^{-1}) of Im@**1** at Different RHs and Temperatures

Temp (°C)	45% RH	60% RH	75% RH	85% RH	93% RH	100% RH
20	7.58×10^{-7}	1.13×10^{-4}	1.43×10^{-4}	9.41×10^{-4}	2.29×10^{-3}	8.91×10^{-3}
30	2.18×10^{-6}	1.79×10^{-4}	2.82×10^{-4}	1.41×10^{-3}	3.07×10^{-3}	1.25×10^{-2}
40	3.62×10^{-6}	2.93×10^{-4}	4.98×10^{-4}	2.41×10^{-3}	4.75×10^{-3}	1.47×10^{-2}
50	6.05×10^{-6}	3.98×10^{-4}	9.31×10^{-4}	3.65×10^{-3}	6.76×10^{-3}	1.83×10^{-2}
60	1.00×10^{-5}	5.61×10^{-4}	1.25×10^{-3}	5.72×10^{-3}	1.00×10^{-3}	2.28×10^{-2}
70	1.51×10^{-5}	9.08×10^{-4}	2.37×10^{-3}	9.48×10^{-3}	1.36×10^{-3}	3.13×10^{-2}
80	3.07×10^{-5}	1.43×10^{-3}	3.78×10^{-3}	1.50×10^{-2}	2.24×10^{-3}	4.00×10^{-2}

Table S7. Proton Conductivities (S cm^{-1}) of Im@**2** at Different RHs and Temperatures

Temp (°C)	45% RH	60% RH	75% RH	85% RH	93% RH	100% RH
20	3.48×10^{-6}	7.46×10^{-5}	7.66×10^{-4}	5.37×10^{-3}	7.02×10^{-3}	3.06×10^{-2}
30	6.01×10^{-6}	1.06×10^{-4}	1.04×10^{-3}	6.95×10^{-3}	9.50×10^{-3}	3.58×10^{-2}
40	1.15×10^{-5}	1.58×10^{-4}	1.39×10^{-3}	8.59×10^{-3}	1.23×10^{-2}	4.06×10^{-2}

50	1.61×10^{-5}	2.42×10^{-4}	1.74×10^{-3}	1.04×10^{-2}	1.66×10^{-2}	4.65×10^{-2}
60	2.49×10^{-5}	3.22×10^{-4}	2.47×10^{-3}	1.23×10^{-2}	2.08×10^{-2}	5.64×10^{-2}
70	4.43×10^{-5}	4.12×10^{-4}	3.07×10^{-3}	1.84×10^{-2}	2.98×10^{-2}	6.33×10^{-2}
80	7.64×10^{-5}	5.41×10^{-4}	4.55×10^{-3}	2.10×10^{-2}	3.77×10^{-2}	7.11×10^{-2}

Table S8. Proton Conductivities (S cm^{-1}) of Im@**3** at Different RHs and Temperatures

Temp (°C)	45% RH	60% RH	75% RH	85% RH	93% RH	100% RH
20	8.13×10^{-5}	3.14×10^{-4}	1.07×10^{-3}	7.38×10^{-3}	1.94×10^{-2}	9.29×10^{-2}
30	1.04×10^{-4}	5.20×10^{-4}	1.48×10^{-3}	8.96×10^{-3}	2.32×10^{-2}	1.09×10^{-1}
40	1.26×10^{-4}	7.01×10^{-4}	2.08×10^{-3}	1.22×10^{-2}	2.79×10^{-2}	1.25×10^{-1}
50	1.89×10^{-4}	9.62×10^{-4}	2.72×10^{-3}	1.40×10^{-2}	3.26×10^{-2}	1.65×10^{-1}
60	2.67×10^{-4}	1.68×10^{-3}	3.53×10^{-3}	1.96×10^{-2}	4.01×10^{-2}	1.91×10^{-1}
70	3.74×10^{-4}	2.25×10^{-3}	4.84×10^{-3}	2.57×10^{-2}	4.59×10^{-2}	2.21×10^{-1}
80	9.35×10^{-4}	2.64×10^{-3}	6.93×10^{-3}	2.90×10^{-2}	5.53×10^{-2}	2.55×10^{-1}

Table S9. Comparison of the σ Values and E_a of **1-3**, Im@**1-3** and Other High-Performing Proton Conducting Materials

Materials	Conductivity (S cm^{-1})	E_a (eV)	Condition	References
Im@MOF-808	3.45×10^{-2}	0.25	65 °C, 99% RH	1
Im@(NENU-3)	1.82×10^{-2}	0.57	70 °C, 90% RH	2
Im-Fe-MOF	1.21×10^{-2}	0.44	60 °C, 98% RH	3
Im@Fe-MOF	4.23×10^{-3}	0.57	60 °C, 98% RH	
Im@UiO-67	1.44×10^{-3}	0.36	120 °C, anhydrous	4
Im@TPB-DMTP-COF	4.37×10^{-3}	/	130 °C, anhydrous	5
Nafion	5.00×10^{-2}	0.22	30 °C, 98% RH	6
PCMOF-3	3.50×10^{-5}	0.17	25 °C, 98% RH	7
Fe(OH)(bdc-(COOH)$_2$)	7.00×10^{-4}	0.21	80 °C, 95% RH	8
In-IA-2D-1	3.40×10^{-3}	0.61	27 °C, 98% RH	9
In-IA-2D-2	2.60×10^{-5}	0.48	90 °C, 98% RH	
PCMOF-5	2.51×10^{-3}	0.16	60 °C, 98% RH	10

PCMOF2½	2.10×10^{-2}	0.21	85 °C, 90% RH	11
IM-UiO-66-AS	1.54×10^{-1}	0.20	80 °C, 98% RH	12
ZIF-8	4.60×10^{-4}	1.14	94 °C, 98% RH	13
PCMOF10	3.55×10^{-2}	0.4	70 °C, 95% RH	14
UiO-66(SO$_3$H)$_2$	8.40×10^{-2}	0.32	80 °C, 90% RH	15
UiO-66(Zr)-(CO$_2$H)$_2$	2.30×10^{-3}	0.17	90 °C, 95% RH	16
VNU-15	2.90×10^{-2}	0.22	95 °C, 60% RH	17
Fe-CAT-5	5.00×10^{-2}	0.24	25 °C, 98% RH	18
MIP-202(Zr)	1.10×10^{-2}	0.22	90 °C, 95% RH	19
MOF-801-Hf	3.90×10^{-3}	0.35	100 °C, 98% RH	
Im@MOF-801-Hf	1.46×10^{-2}	0.53	100 °C, 98% RH	20
DUT-67(Zr)	2.98×10^{-3}	0.25	100 °C, 98% RH	
DUT-67(Hf)	3.86×10^{-3}	0.27	50 °C, 98% RH	21
MIL-163	2.10×10^{-3}	0.25	90 °C, 95% RH	22
Hf-UiO-66-NH$_2$	1.10×10^{-3}	0.52	100 °C, 98% RH	
Hf-UiO-66-(OH)$_2$	4.22×10^{-3}	0.27	100 °C, 98% RH	
Hf-UiO-66	1.79×10^{-3}	0.47	100 °C, 98% RH	
Im@Hf-UiO-66-NH$_2$	1.32×10^{-2}	0.16	100 °C, 98% RH	23
Im@Hf-UiO-66-(OH)$_2$	1.32×10^{-2}	0.36	100 °C, 98% RH	
Im@Hf-UiO-66	1.15×10^{-2}	0.40	100 °C, 98% RH	
BUT-8(Cr)A	1.27×10^{-1}	0.11	80 °C, 100% RH	
BUT-8(Cr)	4.63×10^{-2}	0.21	80 °C, 100% RH	24
Co-MOF-74	4.5×10^{-3}	0.12	90 °C, 95% RH	25
1	1.39×10^{-2}	0.213	80 °C, 100% RH	
Im@**1**	4.00×10^{-2}	0.205	80 °C, 100% RH	
2	2.98×10^{-2}	0.153	80 °C, 100% RH	This work
Im@**2**	7.11×10^{-2}	0.104	80 °C, 100% RH	
3	5.57×10^{-2}	0.121	80 °C, 100% RH	

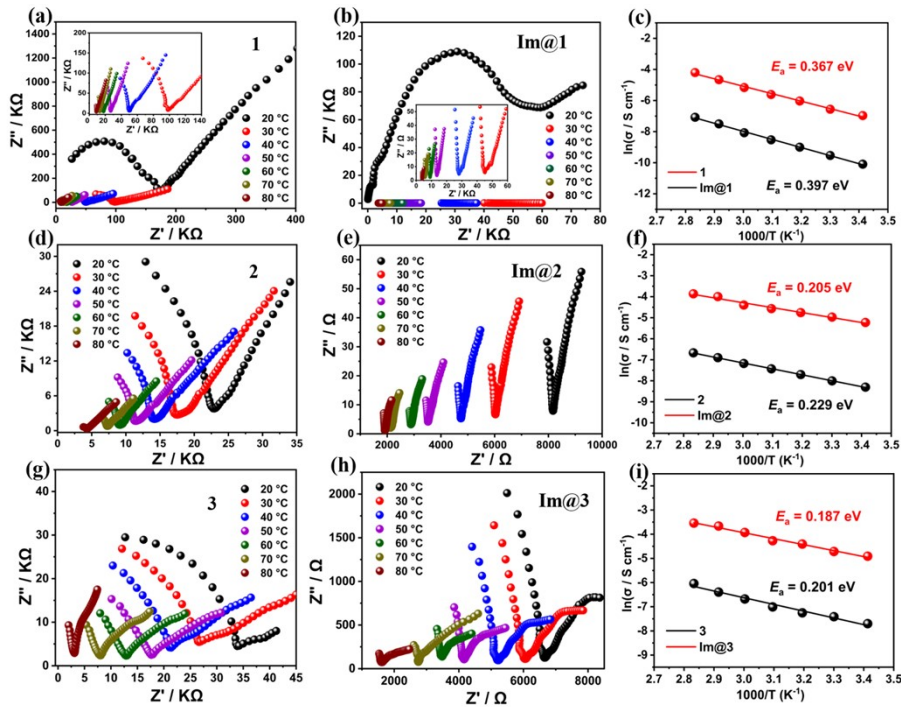| Im@**3** | 2.55×10^{-1} | 0.101 | 80 °C, 100% RH |
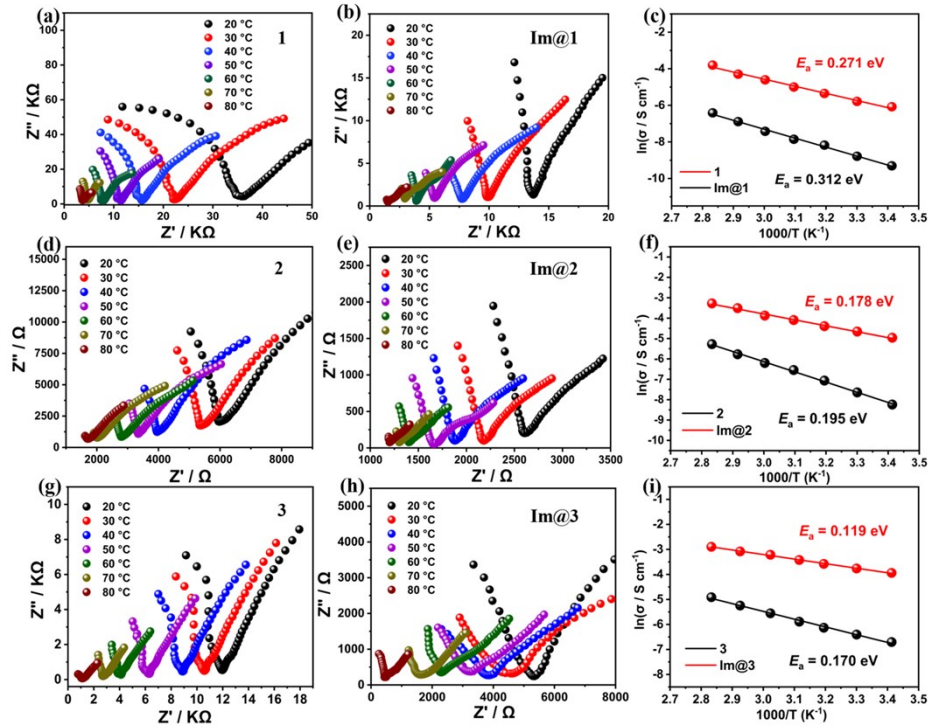
Figure S14. Impedance spectra of **1** (a) and Im@**1** (b); **2** (d) and Im@**2** (e); **3** (g) and Im@**3** (h). Arrhenius plots of proton conductivities for **1** and Im@**1** (c); **2** and Im@**2** (f); **3** and Im@**3** (i) under 93% RH condition with different temperatures.
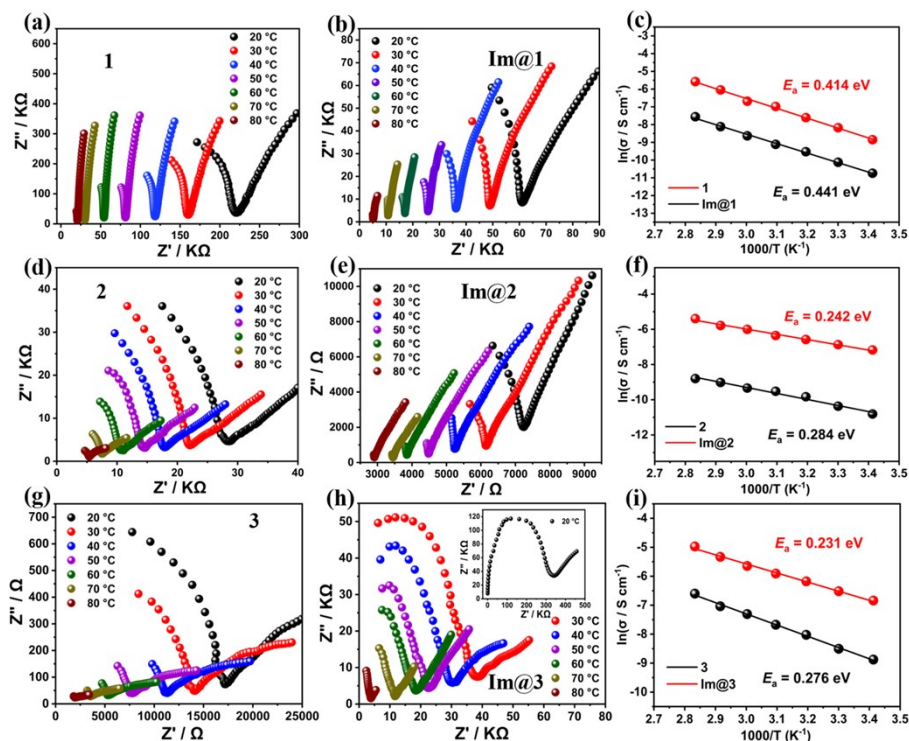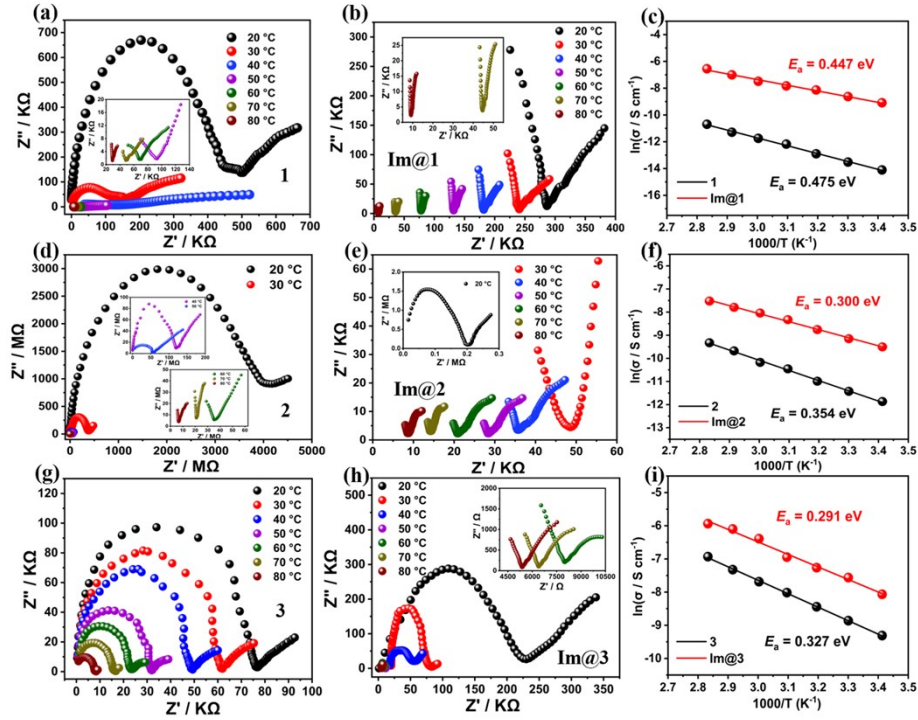
Figure S15. Impedance spectra of **1** (a) and Im@**1** (b); **2** (d) and Im@**2** (e); **3** (g) and Im@**3** (h). Arrhenius plots of proton conductivities for **1** and Im@**1** (c); **2** and Im@**2** (f); **3** and Im@**3** (i) under 86% RH condition with different temperatures.

Figure S16. Impedance spectra of **1** (a) and Im@**1** (b); **2** (d) and Im@**2** (e); **3** (g) and Im@**3** (h). Arrhenius plots of proton conductivity for **1** and Im@**1** (c); **2** and Im@**2** (f); **3** and Im@**3** (i) under 75% RH condition with different temperatures.

Figure S17. Impedance spectra of **1** (a) and Im@**1** (b); **2** (d) and Im@**2** (e); **3** (g) and Im@**3** (h). Arrhenius plots of proton conductivities for **1** and Im@**1** (c); **2** and Im@**2** (f); **3** and Im@**3** (i) under 60% RH condition with different temperatures.
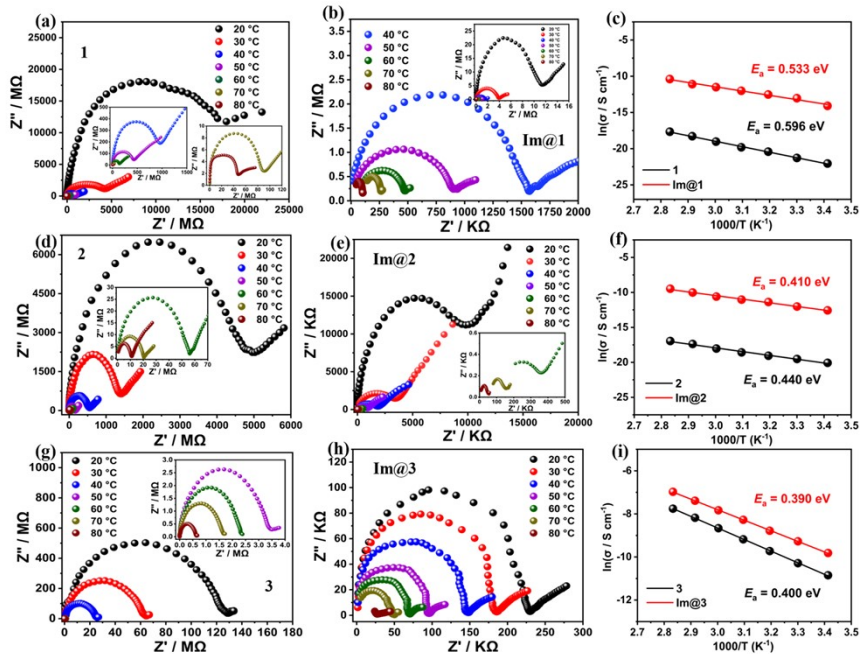
Figure S18. Impedance spectra of **1** (a) and Im@**1** (b); **2** (d) and Im@**2** (e); **3** (g) and Im@**3** (h). Arrhenius plots of proton conductivities for **1** and Im@**1** (c); **2** and Im@**2** (f); **3** and Im@**3** (i) under 45% RH condition with different temperatures.
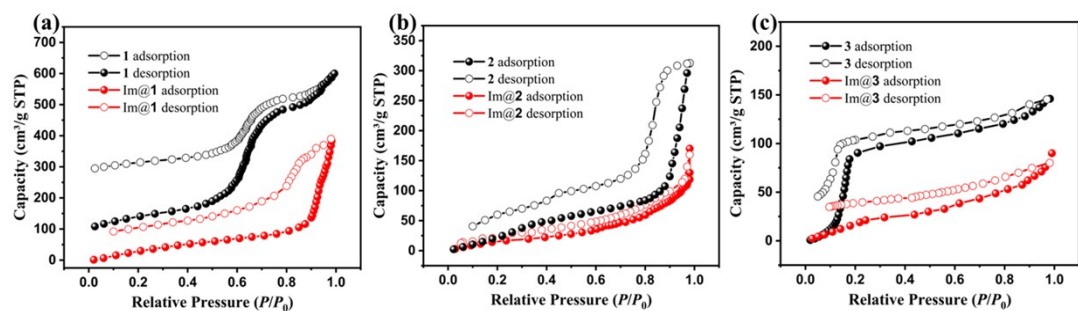
Figure S19. Water vapor adsorption-desorption isotherms of **1** and Im@**1** (a), **2** and Im@**2** (b), **3** and Im@**3** (c) at 298 K.
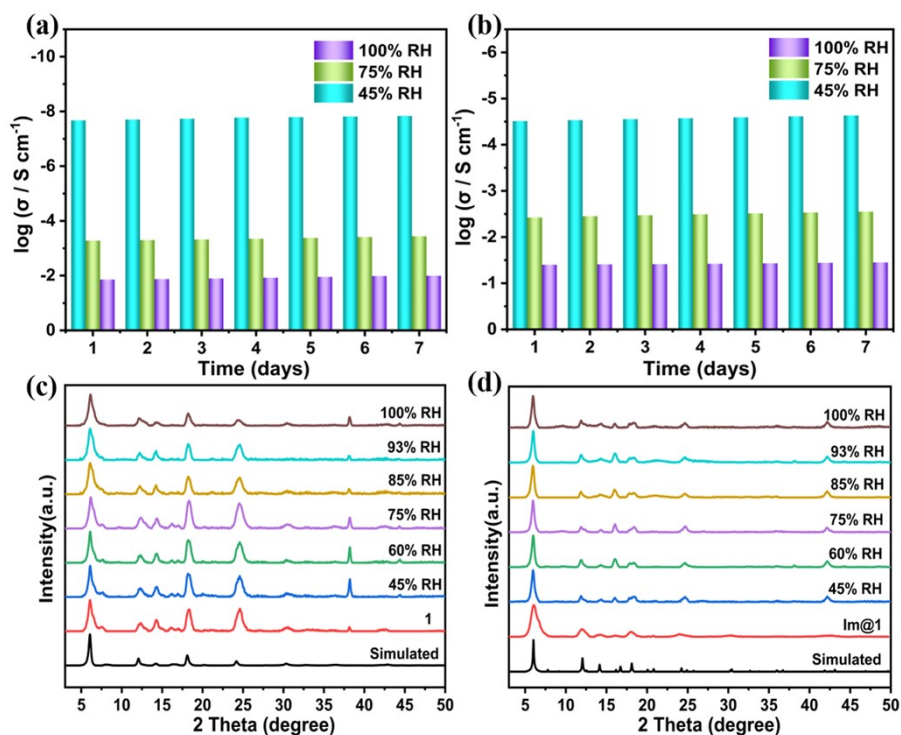

Figure S20. Proton conductivity persistence of **1** (a), and Im@**1** (b) at 100% RH, 75% RH, and 45% RH. PXRD patterns after impedance measurements (c), and (d).

Figure S21. Proton conductivity persistence of **2** (a), and Im@**2** (b) at 100% RH, 75% RH, and 45% RH. PXRD patterns after impedance measurements (c), and (d).
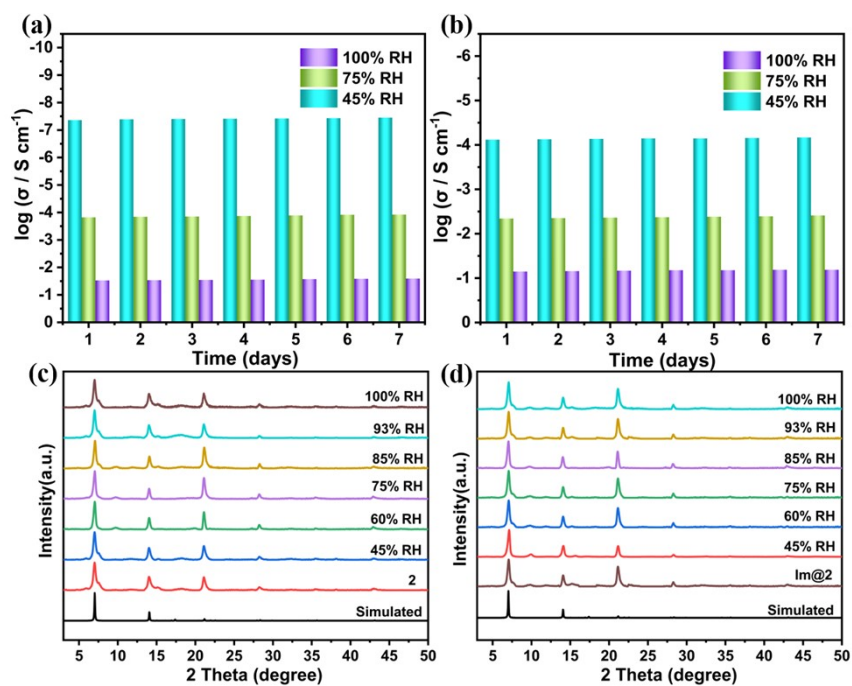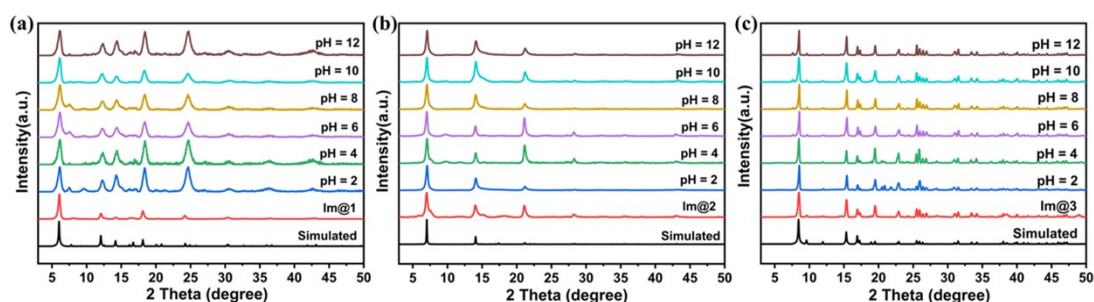

Figure S22. The PXRD patterns of simulated, synthesized Im@**1-3** and the samples of Im@**1-3** underwent proton conduction tests and were then immersed in aqueous solutions at different pH for 24 h.
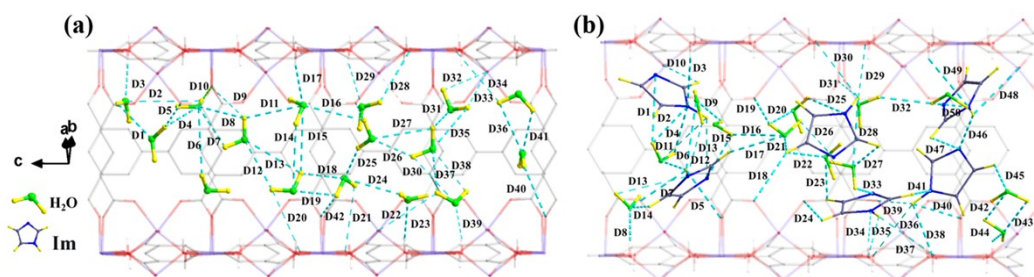

Figure S23. The hydrogen-bonding distances of **3** (a), and Im@**3** (b) range from 1.8 to 3.5 Å (thick dotted line), and from 3.5 to 4.0 Å (thin dotted line). (The H atom of MOFs has been omitted for clarity).

Table S10. Hydrogen-bonding and distances in **3**

Hydrogen-bonding	Distance (Å)	Hydrogen bonding	Distance (Å)	Hydrogen-bonding	Distance (Å)
D1	3.469	D15	2.804	D29	3.684
D2	3.942	D16	2.994	D30	3.655
D3	2.982	D17	2.908	D31	3.351
D4	3.076	D18	2.975	D32	3.808
D5	3.835	D19	3.421	D33	3.921
D6	2.430	D20	3.735	D34	3.697
D7	3.426	D21	3.892	D35	3.017
D8	3.253	D22	3.915	D36	3.230
D9	3.648	D23	3.469	D37	2.653
D10	3.973	D24	2.763	D38	3.931
D11	2.719	D25	2.813	D39	3.770
D12	3.012	D26	3.471	D40	3.165
D13	3.443	D27	3.071	D41	3.312
D14	3.334	D28	1.861	D42	2.642

Table S11. Hydrogen bonding and distances in Im@**3**

Hydrogen-bonding	Distance (Å)	Hydrogen-bonding	Distance (Å)	Hydrogen-bonding	Distance (Å)
D1	1.804	D19	3.402	D37	3.574
D2	3.035	D20	2.135	D38	2.791
D3	2.864	D21	2.642	D39	3.882
D4	2.848	D22	2.775	D40	2.491
D5	3.312	D23	2.169	D41	2.453
D6	3.001	D24	2.853	D42	3.029
D7	3.327	D25	3.503	D43	2.362
D8	2.568	D26	3.921	D44	2.711
D9	3.420	D27	1.827	D45	3.385
D10	3.913	D28	3.265	D46	3.084
D11	3.940	D29	3.518	D47	3.384

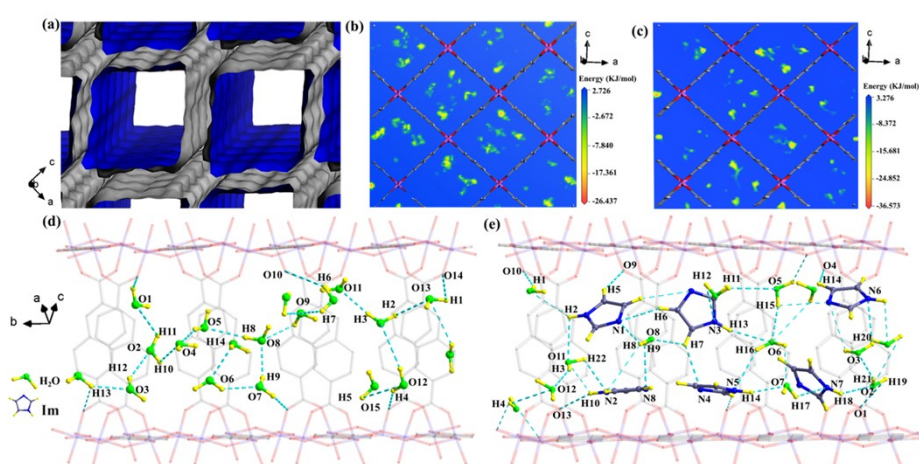|					
D12	3.834	D30	3.522	D48	3.303
D13	3.764	D31	3.902	D49	3.382
D14	3.408	D32	3.057	D50	2.729
D15	1.882	D33	2.679		
D16	3.135	D34	3.610		
D17	2.665	D35	3.547		
D18	2.817	D36	3.543		

Figure S24. Surface view of the porous structure of **2** along the crystallographic *b* axis (a). Slices of the potential field for water (b), and imidazole (c) molecules in **2** along the *b* axis. Diagrams of hydrogen-bonding networks in the **2** (d), and Im@**2** (e) channels along the *b* axis by GCMC simulations. The hydrogen-bonding distances range from 2.4 to 3.5 Å (thick dotted line), and from 3.5 to 4.0 Å (thin dotted line). (The H atom of MOFs has been omitted for clarity).
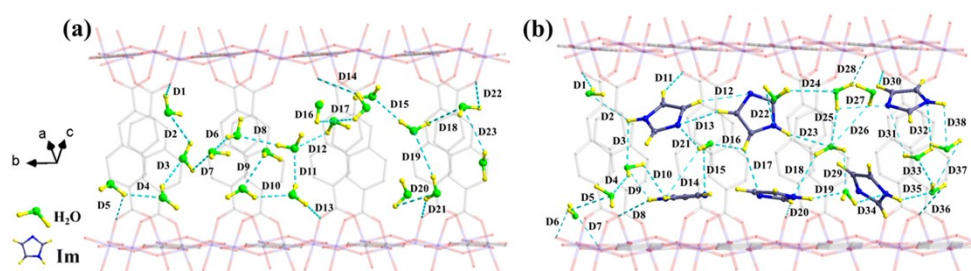

Figure S25. The hydrogen-bonding distances of **2** (a), and Im@**2** (b) range from 2.4 to 3.5 Å (thick dotted line), and from 3.5 to 4.0 Å (thin dotted line). (The H atom of MOFs has been omitted for clarity).

Table S12. Hydrogen-bonding and distances in **2**

Hydrogen-bonding	Distance (Å)	Hydrogen-bonding	Distance (Å)	Hydrogen-bonding	Distance (Å)
D1	3.243	D9	3.053	D17	2.699
D2	2.911	D10	3.841	D18	2.790
D3	2.910	D11	3.252	D19	3.823
D4	3.720	D12	3.859	D20	3.317
D5	3.921	D13	3.951	D21	3.177
D6	2.484	D14	3.339	D22	3.421
D7	3.447	D15	3.395	D23	3.788
D8	3.243	D16	3.811		

Table S13. Hydrogen-bonding and distances in Im@**2**

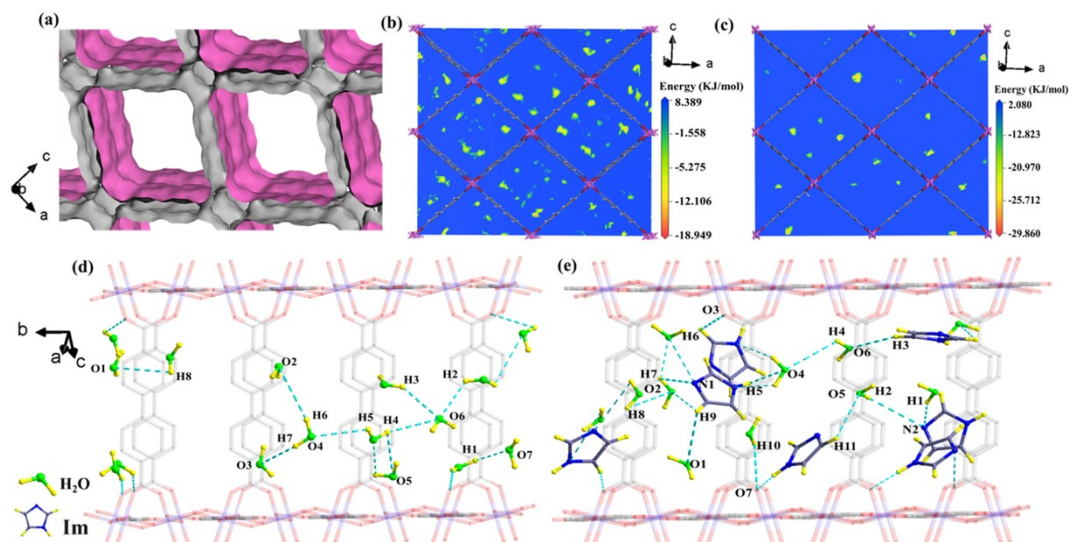| Hydrogen-bonding	Distance (Å)	Hydrogen-bonding	Distance (Å)	Hydrogen-bonding	Distance (Å)
D1	3.440	D14	3.820	D27	3.689
D2	3.764	D15	3.490	D28	3.733
D3	2.644	D16	3.430	D29	3.824
D4	2.975	D17	2.879	D30	3.435
D5	2.640	D18	3.439	D31	3.927
D6	3.950	D19	3.431	D32	3.376
D7	2.902	D20	3.792	D33	2.823
D8	2.434	D21	3.267	D34	3.452
D9	3.851	D22	3.083	D35	3.427
D10	3.821	D23	3.435	D36	3.494
D11	2.746	D24	3.471	D37	3.870
D12	3.684	D25	3.413	D38	3.762
D13	3.055	D26	3.741		

Figure S26. Surface view of the porous structure of **1** along the crystallographic *b* axis (a). Slices of the potential field for water (b), and imidazole (c) molecules in **1** along the *b* axis. Diagrams of hydrogen-bonding networks in the **1** (d), and Im@**1** (e) channels along the *b* axis by GCMC simulations. The hydrogen-bonding distances range from 3.1 to 3.5 Å (thick dotted line), and from 3.5 to 4.0 Å (thin dotted line). (The H atom of MOFs has been omitted for clarity).
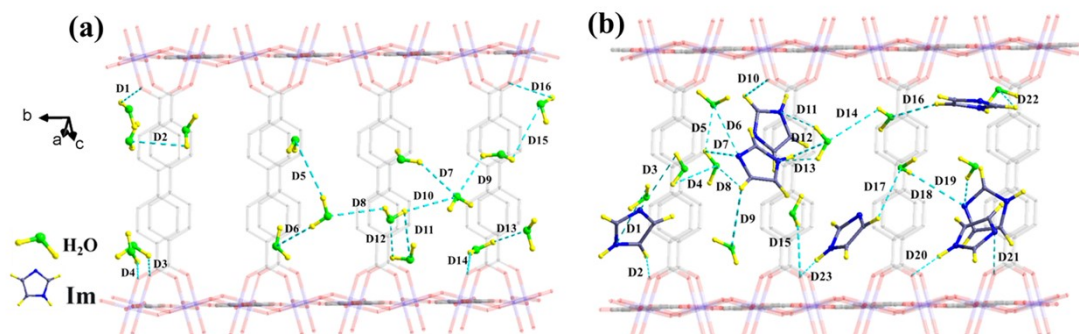

Figure S27. The hydrogen-bonding distances of **1** (a), and Im@**1** (b) range from 3.1 to 3.5 Å (thick dotted line), and from 3.5 to 4.0 Å (thin dotted line). (The H atom of MOFs has been omitted for clarity).

Table S14. Hydrogen bonding and distance in **1**

Hydrogen-Bonding	Distance (Å)	Hydrogen-Bonding	Distance (Å)	Hydrogen-Bonding	Distance (Å)
D1	3.944	D7	3.593	D13	3.528
D2	3.530	D8	3.589	D14	3.923

Hydrogen-bonding	Distance (Å)	Hydrogen-bonding	Distance (Å)	Hydrogen-bonding	Distance (Å)
D3	3.926	D9	3.502	D15	3.878
D4	3.890	D10	3.549	D16	3.862
D5	3.480	D11	3.496		
D6	3.284	D12	3.711		

Table S15. Hydrogen-bonding and distances in Im@**1**

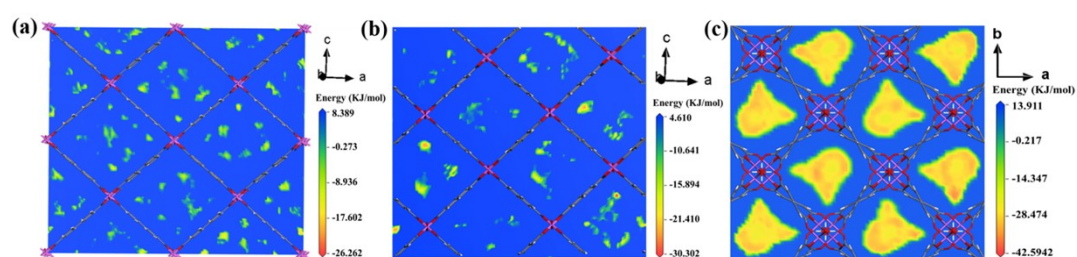| Hydrogen-bonding	Distance (Å)	Hydrogen-bonding	Distance (Å)	Hydrogen-bonding	Distance (Å)
D1	3.795	D10	3.252	D19	3.908
D2	3.358	D11	3.219	D20	3.343
D3	3.998	D12	2.537	D21	3.583
D4	3.485	D13	3.644	D22	3.681
D5	3.270	D14	3.390	D23	3.652
D6	3.058	D15	3.086	D24	3.286
D7	3.290	D16	3.896	D25	3.631
D8	3.886	D17	3.492	D26	3.758
D9	3.116	D18	3.798		

Figure S28. Slices of the potential field for water and imidazole molecules in **1** (a), **2** (b) along the *b* axis and in **3** (c) along the *c* axis.

6. References.

1 H. B. Luo, Q. Ren, P. Wang, J. Zhang, L. Wang and X. M. Ren, High Proton Conductivity Achieved by Encapsulation of Imidazole Molecules into Proton-Conducting MOF-808, *ACS Appl. Mater. Inter.*, 2019, **11**(9), 9164-9171.

2 Y. Ye, W. Guo, L. Wang, Z. Li, Z. Song, J. Chen, Z. Zhang, S. Xiang, and B. Chen, Straightforward Loading of Imidazole Molecules into Metal-Organic Framework

for High Proton Conduction, *J. Am. Chem. Soc.*, 2017, **139**(44), 15604-15607.

3   F. M. Zhang, L. Z. Dong, J. S. Qin, W. Guan, J. Liu, S. L. Li, M. Lu, Y. Q. Lan, Z. M. Su and H. C. Zhou, Effect of Imidazole Arrangements on Proton-Conductivity in Metal-Organic Frameworks, *J. Am. Chem. Soc.*, 2017, **139**(17), 6183-6189.

4   S. Liu, Z. Yue and Y. Liu, Incorporation of Imidazole within the Metal-Organic Framework UiO-67 for Enhanced Anhydrous Proton Conductivity, *Dalton Trans*., 2015, **44**, 12976-12980.

5   H. Xu, S. Tao and D. Jiang, Proton Conduction in Crystalline and porous Covalent Organic Frameworks, *Nat. Mater*., 2016, **15**, 722-726.

6   Y. Prykhodko, K. Fatyeyeva, L. Hespel and S. Marais, Progress in hybrid composite Nafion®-based membranes for proton exchange fuel cell application, *Chem. Eng. J.*, 2021, **409**(1), No. 127329.

7   J. M. Taylor, R. K. Mah, I. L. Moudrakovski, C. I. Ratcliffe, R. Vaidhyanathan and G. K. H. Shimizu, Facile proton conduction via ordered water molecules in a phosphonate metal-organic framework, *J. Am. Chem. Soc.*, 2010, **132**(40), 14055-14057.

8   A. Shigematsu, T. Yamada and H. Kitagawa, Wide control of proton conductivity in porous coordination polymers, *J. Am. Chem. Soc.*, 2011, **133**(7), 2034-2036.

9   T. Panda, T. Kundu and R. Banerjee, Structural isomerism leading to variable proton conductivity in indium(iii) isophthalic acid based frameworks, *Chem. Commun*., 2013, **49**(55), 6197-6199.

10 J. M. Taylor, K. W. Dawson and G. K. H. Shimizu, A water-stable metal-organic framework with highly acidic pores for proton-conducting applications, *J. Am. Chem. Soc.*, 2013, **135**(4), 1193-1196.

11 S. R.; Kim, K. W. Dawson, B. S. Gelfand, J. M. Taylor and G. K. H. Shimizu, Enhancing Proton Conduction in a Metal-Organic Framework by Isomorphous Ligand Replacement, *J. Am. Chem. Soc*., 2013, **135**(3), 963-966.

12 X.-M. Li, J. Liu, C. Zhao, J.-L. Zhou, L. Zhao, S.-L. Li and Y.-Q. Lan, Strategic hierarchical improvement of superprotonic conductivity in a stable metal-organic framework system, *J. Mater. Chem. A*, 2019, **7**, 25165-25171.

13 P. Barbosa, N. C. Rosero-Navarro, F. N. Shi and F. M. L. Figueiredo, Protonic Conductivity of Nanocrystalline Zeolitic Imidazolate Framework 8, *Electrochim. Acta*, 2015, **153**(20), 19-27.

14 P. Ramaswamy, N. E. Wong, B. S. Gelfand and G. K. H. Shimizu, A Water Stable Magnesium MOF That Conducts Protons over 10^{-2} S cm^{-1}, *J. Am. Chem. Soc.*, 2015, **137**(24), 7640-7643.

15 W. J. Phang, H. Jo, W. R. Lee, J. H. Song, K. Yoo, B. S. Kim and C. S. Hong, Superprotonic Conductivity of a UiO-66 Framework Functionalized with Sulfonic Acid Groups by Facile Postsynthetic Oxidation, *Angew. Chem. Int. Ed.*, 2015, **54**(17), 5142-5146.

16 D. D. Borges, S. Devautour-Vinot, H. Jobic, J. Ollivier, F. Nouar, R. Semino, T. Devic, C. Serre, F. Paesani and G. Maurin, Proton Transport in a Highly Conductive Porous Zirconium-Based Metal-Organic Framework: Molecular Insight, *Angew. Chem. Int. Ed.*, 2016, **55**(12), 3919-3924.

17 T. N. Tu, Phan, N. Q.; Vu, T. T.; Nguyen, H. L.; Cordova, K. E.; Furukawa, H. High proton conductivity at low relative humidity in an anionic Fe-based metal-organic framework, *J. Mater. Chem. A.*, 2016, **4**, 3638-3641.

18 N. T. T. Nguyen, H. Furukawa, F. Gándara, C. A. Trickett, H. M. Jeong, K. E. Cordova and O. M. Yaghi, Three-Dimensional Metal-Catecholate Frameworks and Their Ultrahigh Proton Conductivity, *J. Am. Chem. Soc.*, 2015, **137**(49), 15394-15397.

19 S. Wang, M. Wahiduzzaman, L. Davis, A. Tissot, W. Shepard, J. Marrot, C. Martineau-Corcos, D. Hamdane, G. Maurin, S. Devautour-Vinot and C. Serre, A robust zirconium amino acid metalorganic framework for proton conduction, *Nat. Commun.*, 2018, **9**, 4937-4944.

20 H. M. Ren, Y. R. Liu, B. Y. Liu, Z. F. Li and G. Li, Comparative studies on the proton conductivities of hafnium-based metal-organic frameworks and related chitosan or nafion composite membranes, *Inorg. Chem.*, 2022, **61**(25), 9564-9579.

21 L. L. Kang, C. Xing, Y. X. Jin, L. X. Xie, Z. F. Li and G. Li, Two dual-function Zr/Hf-MOFs as high-performance proton conductors and amines impedance sensors, *Inorg. Chem.*, 2023, **62**, 3036-3046.

22 P. G. M. Mileo, S. Devautour-Vinot, G. Mouchaham, F. Faucher, N. Guillou, A. Vimont, C. Serre and G. Maurin, Protonconducting phenolate-based Zr metal-organic framework: a joint experimental-modeling investigation, *J. Phys. Chem. C*, 2016, **120**(43), 24503-24510.

23 X. Chen, S.-Z. Wang, S.-H. Xiao, Z.-F. Li and G. Li, High Protonic Conductivity of Three Highly Stable Nanoscale Hafnium(IV) Metal-Organic Frameworks and Their Imidazole-Loaded Products, *Inorg. Chem*., 2022, **61**(12), 4938-4947.

24 F. Yang, G. Xu, Y. Dou, B. Wang, H. Zhang, H. Wu, W. Zhou, J.-R. Li and B. Chen, A flexible metal-organic framework with a high density of sulfonic acid sites for proton conduction, *Nat. Energy*, 2017, **2**, 877-883.

25 S. Hwang, E. J. Lee, S. Dahae and N. C. Jeong, High proton mobility with high directionality in isolated channels of MOF-74, *ACS Appl. Mater. Inter.*, 2018, **10**(41), 35354-35360.